

# Monocular pose estimation of articulated surgical instruments in open surgery

Robert Spektor<sup>a</sup>, Tom Friedman<sup>b</sup>, Itay Or<sup>b</sup>, Gil Bolotin<sup>b</sup>, Shlomi Laufer<sup>a</sup>

<sup>a</sup>Faculty of Data and Decision Sciences, Technion - Israel Institute of Technology, Haifa, Israel

<sup>b</sup>Rambam Health Care Campus, Haifa, Israel

---

## ABSTRACT

### Abstract

This work presents a novel approach to monocular 6D pose estimation of surgical instruments in open surgery, addressing challenges such as object articulations, symmetries, occlusions, and lack of annotated real-world data. The method leverages synthetic data generation and domain adaptation techniques to overcome these obstacles. The proposed approach consists of three main components: (1) synthetic data generation using 3D modeling of surgical tools with articulation rigging and physically-based rendering; (2) a tailored pose estimation framework combining object detection with pose estimation and a hybrid geometric fusion strategy; and (3) a training strategy that utilizes both synthetic and real unannotated data, employing domain adaptation on real video data using automatically generated pseudo-labels. Evaluations conducted on videos of open surgery demonstrate the good performance and real-world applicability of the proposed method, highlighting its potential for integration into medical augmented reality and robotic systems. The approach eliminates the need for extensive manual annotation of real surgical data.

## 1. Introduction

Object pose estimation is a fundamental problem in computer vision that aims to determine the position and orientation of an object in 3D space relative to a camera. It has a wide range of applications, including robotic manipulation Tremblay et al. [57], autonomous navigation [41], and augmented reality [50]. In the medical domain, accurate pose estimation of surgical instruments plays a crucial role in computer-assisted surgery, enabling advanced features such as surgical navigation, skill assessment, and robotic assistance [13, 7, 17].

Traditional approaches to object pose estimation often rely on template matching [58, 45] or key-point matching [31]. However, with the advent of deep learning, significant progress has been made in developing more robust and accurate pose estimation techniques using various input modalities, including RGB images [62, 47], depth maps, and point clouds [59].

Existing approaches to object pose estimation can be broadly categorized into two groups: marker-based [39, 1] and markerless methods. Marker-based methods rely on attaching physical markers, such as color-coded fiducials [61] or passive reflective markers [18], to the instruments. These markers are then detected and tracked in the image space to estimate the pose. While marker-based methods can provide accurate pose estimates, they require modifying the instruments and may interfere with the surgical workflow [10].

On the other hand, markerless methods aim to estimate the pose directly from the visual appearance of the instruments in the image. These methods typically involve training deep neural networks on large datasets of annotated images. The networks learn to extract relevant features and estimate the 6D pose of the instruments using various techniques, such as landmark detection [46] or dense correspondence estimation with Perspective-n-Point (PnP) algorithm [51], or direct pose regression [60]. Markerless methods offer a more practical and non-intrusive solution for surgical instrument pose estimation, as they do not require any modifications to the instruments.

While markerless pose estimation methods have shown promising results, they face several challenges that hinder their widespread adoption in surgical settings. One of the primary challenges is the scarcity of annotated real-world data [3, 9]. Collecting and annotating large datasets of images with accurate 6D pose labels is time-consuming, expensive, and often impractical [25, 57]. This challenge is particularly relevant in the medical domain, where privacy concerns and the difficulty of recording during surgeries due to camera placement restrictions (as some areas must remain sterile) further complicate the data collection process.

To address the data scarcity problem, researchers have explored the use of synthetic data generation techniques [56, 57]. By creating realistic virtual models of surgical instruments and rendering them in simulated environments, large amounts of annotated training data can be generated efficiently. However, models trained solely on synthetic data often suffer from the domain gap problem, where the learned features do not generalize well to real-world scenarios. To bridge this gap, domain adaptation techniques, such as domain randomization [57] and

---

*e-mail:* spektor@campus.technion.ac.il (Robert Spektor),  
t\_friedman@rmabam.health.gov.il (Tom Friedman),  
i\_or@rmabam.health.gov.il (Itay Or),  
g\_bolotin@rmabam.health.gov.il (Gil Bolotin),  
laufer@technion.ac.il (Shlomi Laufer)

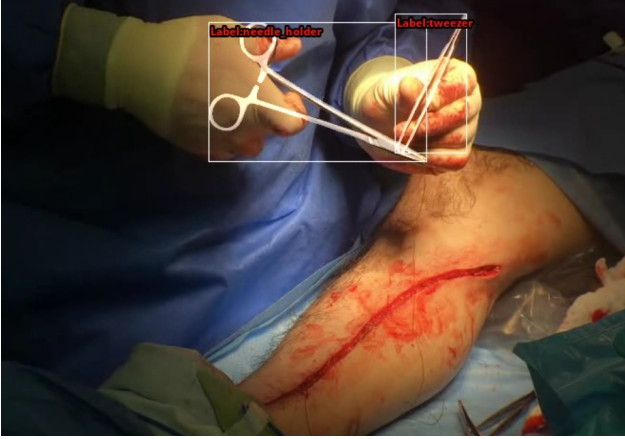


Fig. 1. Pose estimation of surgical instruments, showcasing the precision required in labeling articulated tools, such as needle holders and tweezers, during an open surgical procedure.



Fig. 2. Surgical instruments with reflective surface

adversarial training [4], have been proposed. These techniques aim to make the models more robust to the differences between synthetic and real data, improving their performance on real-world images.

Despite the significant progress in deep learning-based pose estimation methods, their application to surgical instruments poses additional challenges due to the unique characteristics of the surgical environment and the instruments themselves [42, 15]. Surgical instruments often have metallic and reflective surfaces, which can cause severe specular reflections and make it difficult to extract reliable visual features. Moreover, articulated objects, such as surgical instruments with movable parts, introduces additional complexities. Articulated objects have multiple degrees of freedom, allowing their parts to move independently, which significantly increases the difficulty of accurately estimating their pose.

In this study, we tackle the multiple challenges raised by of open surgery pose detection. Our key contributions include:

1. Creation of a new in-the-wild dataset of open surgery tool and hand segmentations.
2. Development of a synthetic dataset for tool pose estimation

that addresses issues like tool articulation and hand occlusions.

3. Utilization of solely synthetic data to develop methods for both object detection and tool pose estimation. The pose estimation incorporates the standard six degrees of freedom as well as tool articulation (i.e., measuring how open the tools are).
4. Introduction of a sim2real domain adaptation technique that utilizes the temporal-spatial characteristics of video data to refine both object detection and pose estimation models, with each model helping to improve the other.

It is important to highlight that our approach eliminates the need for manual data labeling. New tools can be added to the dataset using only their 3D models (e.g., STL files) without manual labeling. Any labeling done in this study serves solely to validate our algorithms. Addressing these challenges is crucial for developing accurate and reliable pose estimation methods for surgical instruments, which can ultimately lead to improved surgical outcomes and patient care.

## Related Work

### 1.1. Object Pose Estimation Methods

Object pose estimation methods have seen significant advances in recent years, particularly with the rise of deep learning. In this section, we discuss state-of-the-art methods for both general object pose estimation and those specifically designed for surgical instruments. **Single-stage methods** directly regress the 6D pose of an object from the input image. [62] predicts the 3D translation and rotation of an object in a single forward pass. Having separate branches for object classification and pose estimation. The pose estimation branch regresses the 3D translation and rotation in a quaternion representation. [12], extends the popular object detection framework Mask R-CNN [22] to jointly perform object detection and pose estimation. It introduces a pose estimation branch that operates on the region of interest (ROI) features extracted by the ROI pooling layer. It combines object detection and pose estimation in a single network, allowing pose estimation of multiple objects in an image. [64] is a single-stage method that estimates 2D-3D dense correspondence maps on the full image and estimates the pose via PnP-RANSAC. Then, further refine the initial pose estimate using a custom deep learning model.

**Two-stage methods** decouple object detection and pose estimation by first detecting the object of interest and then estimating its pose using a separate network. [47] employs a segmentation-based approach to identify the 2D centers of the objects of interest. The segmentation network does not use a hourglass-shaped architecture, making it more efficient. It then predicts the 3D bounding box of the object and regresses the 6D pose from the cropped object image. The method employs a coarse-to-fine approach, where the initial pose estimate is refined using a more precise network.

[32] disentangles the pose estimation process into predicting the object's rotation and translation separately. This disentanglement reportedly leads to more accurate and robust pose estimation compared to previous methods.

[44] employs a fully convolutional network to predict dense 2D-3D correspondences and utilizes a GAN to enhance the stability of these dense correspondences.

[46] presents a voting-based approach to manage occluded or truncated keypoints. Each pixel votes for the object’s keypoints, and the pose is determined by solving a least-squares problem. The network generates pixel-wise heatmaps for each keypoint and employs a differentiable RANSAC layer to estimate the pose from the keypoint correspondences.

Several state-of-the-art deep learning architectures have been proposed to further improve the accuracy and robustness of object pose estimation.

[51] focuses on surface encoding by assigning a unique code to each vertex on a 3D object model, starting with coarse fragments and refining to finer details. The method includes assigning these unique codes to 3D vertices, predicting their correspondence to image pixels, and estimating the object’s pose using a PnP-RANSAC-like approach.

[60] employs a direct regression approach to efficiently and differentially predict the 6D pose of an object in an end-to-end trainable manner. By utilizing intermediate geometric representations, the method guides and enhances the accuracy of pose prediction. It achieves competitive performance compared to state-of-the-art methods on standard benchmarks.

While these methods have shown impressive results on general object pose estimation benchmarks, they often struggle when applied directly to surgical instruments due to the unique challenges posed by the surgical environment.

### 1.2. Pose Estimation Methods for Surgical Instruments

Several deep learning-based methods have been proposed specifically for surgical instrument pose estimation, addressing the unique challenges posed by the surgical environment. These methods can be further categorized based on the type of surgery they focus on, such as laparoscopic or open surgery.

**Methods Focusing on Laparoscopic Instruments.** [21] present a method for detection, segmentation, and 3D pose estimation of laparoscopic instruments using CNN’s and algebraic geometry. They employ a two-stage approach, where the instrument is first detected and segmented using a CNN-based segmentation network. The segmented instrument is then processed by a separate CNN to predict its 3D pose using an algebraic geometry-based method. The authors demonstrate the effectiveness of their approach on a dataset of laparoscopic images, achieving high accuracy in instrument detection, segmentation, and pose estimation.

**Methods addressing challenges in open surgery.** [23] introduce a markerless hand-tool tracking pipeline for open surgery, focusing on larger, non-articulated tools. They create a synthetic data generation pipeline using the MANO hand model [49] and GraspIt! [40] simulator to produce realistic hand-tool interactions. The authors also capture real-world data with ground truth annotations in a mock operating room. They evaluate three baseline models ([46], HandObjectNet, and a combined model) trained on the synthetic dataset and refined on the real dataset. The best-performing model, HandObjectNet, achieves an average 3D vertex error of 16.7 mm on the synthetic test set and 13.8 mm on the real test set after refinement.

This work demonstrates the potential of using synthetic data for pretraining and real-world data for fine-tuning pose estimation models in open surgery.

### 1.3. Overview of Synthetic Data Generation for Object Pose Estimation

Synthetic data generation has gained significant attention in the object pose estimation community due to several reasons. First, annotating real-world data for object pose estimation is labor-intensive and error-prone, often requiring specialized equipment or manual labeling by experts. In contrast, synthetic data can be automatically generated with precise annotations, saving time and resources. Second, rendering synthetic data is fast and cheap compared to capturing real-world data, allowing researchers to create large-scale datasets with diverse object appearances, poses, backgrounds, and lighting conditions. This diversity can improve the robustness and generalization of trained object pose estimation models.

One of the most common approaches for generating synthetic data for object pose estimation is through 3D modeling and rendering. This involves creating 3D models of objects using computer graphics software and rendering them from different viewpoints to generate 2D images with corresponding pose annotations. The 3D models can be created manually using 3D modeling software or scanned from real objects using techniques like photogrammetry or depth sensing.

To create realistic synthetic images, physically-based rendering (PBR) techniques are often employed. PBR accurately simulates the flow of light energy in the scene by ray tracing, naturally accounting for complex illumination effects such as scattering, refraction, and reflection [26]. The resulting rendered images look realistic and are often difficult to differentiate from real photographs.

In the context of object pose estimation, 3D models of objects are placed in virtual scenes and rendered from various viewpoints. The precise 3D poses of the objects in these rendered images can be automatically recorded, providing accurate ground-truth annotations for training and evaluating object pose estimation models. By varying the object poses, backgrounds, and lighting conditions in the virtual scenes, researchers can generate diverse synthetic datasets that cover a wide range of scenarios.

The effectiveness of using synthetic data generated through 3D modeling and PBR for object pose estimation has been demonstrated in various studies. In the BOP challenge 2020 on 6D object localization [26], methods trained on PBR images achieved significantly higher accuracy scores compared to those trained on “render & paste” images. While incorporating real training images further improved the scores, competitive results were obtained using only PBR images. Notably, the increased photorealism of PBR images led to clear improvements even for methods that apply strong data augmentation, such as CosyPose [30].

### 1.4. Bridging the Domain Gap Between Synthetic and Real Data

While synthetic data generation has shown great promise in training deep learning models for object pose estimation, there

often exists a domain gap between synthetic and real-world data [57]. This domain gap can limit the performance of models trained solely on synthetic data when applied to real-world scenarios. Various techniques have been proposed to address this issue to bridge the domain gap and improve the transferability of models trained on synthetic data to real-world applications.

Domain adaptation techniques:

1. **Fine-tuning:** One common approach is to fine-tune models that are pre-trained on synthetic data using a smaller dataset of real-world images. This allows the models to adapt to the characteristics of real-world data while leveraging the knowledge learned from synthetic data. Fine-tuning can be performed on the entire model or only on specific layers, depending on the similarity between the synthetic and real-world domains [55, 56].
2. **Unsupervised domain adaptation:** Unsupervised domain adaptation techniques aim to align the feature distributions of synthetic and real-world data without requiring labeled real-world examples. These techniques often involve adversarial training, where a discriminator network is trained to distinguish between features from the synthetic and real-world domains, while the pose estimation network is trained to fool the discriminator. By minimizing the domain discrepancy, unsupervised domain adaptation can improve the performance of object pose estimation models on real-world data [20].

**Examples of bridging the domain gap:** Several works have successfully demonstrated the effectiveness of bridging the domain gap between synthetic and real data for object pose estimation. For instance, the work by [23] on hand-tool interaction in open surgery utilizes a combination of synthetic pre-training and real-world fine-tuning. They first train their models on a large-scale synthetic dataset generated using a physically-based rendering pipeline and then fine-tune the models on a smaller dataset of real-world images captured in a mock operating room. This approach allows them to leverage the diversity and accuracy of synthetic data while adapting the models to the characteristics of real-world surgical scenes.

Another example is the work by Sundermeyer et al. [53], where they propose a self-supervised domain adaptation method for object pose estimation. Their approach relies on a differentiable renderer to generate synthetic views of objects and align them with real-world images using a contrastive loss. By minimizing the domain discrepancy between synthetic and real-world images, their method can improve the performance of object pose estimation models on real-world data without requiring any labeled real-world examples.

### 1.5. Data Collection

We collected real-world data from surgical procedures for the purpose of unsupervised sim-to-real domain adaptation and to validate our approach and ensure its effectiveness in practical surgical scenarios. Data were collected from seven different surgeries. Each surgery involved the removal of a vein from the leg as part of the ‘‘Coronary Artery Bypass Graft (CABG)’’ procedure. Our focus is specifically on the suturing part of the

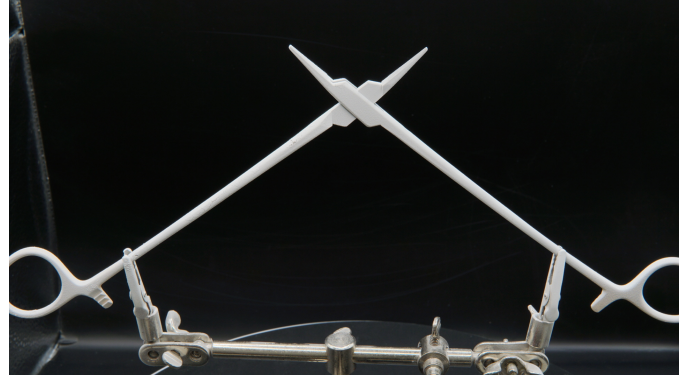


**Fig. 3. Needle-holder photographed on a spinning table for photogrammetry.**

procedure, which typically lasts between 15 to 30 minutes. In total, four different surgeons performed the surgeries, with each suturing procedure carried out by a single surgeon. The study was approved by the Rambam Health Care Campus IRB committee.

### 1.6. Data Annotation for Evaluation

Since annotating 6D pose is very complex, we instead annotate instance segmentation labels and evaluate on them. Approximately 100 images were selected from each procedure, covering a variety of tool poses and challenging scenarios. These frames were manually annotated.

For each selected frame, we created detailed segmentation masks of the surgical tools of interest (needle-holder and tweezers), as well as background surgical tools and hands. These segmentation masks provide pixel-level annotations of the tools and hands in the surgical scene. The annotation process was carried out using the SAM (Segment Anything) model [28], which generates high-quality object masks from input prompts such as points or boxes. Any masks that did not meet quality standards were manually adjusted. These annotated frames provide essential ground truth data for evaluating the effectiveness of our pose estimation network on actual surgical data.

## 2. Methodology

### 2.1. Overview of the Proposed Pipeline

The proposed pipeline addresses the unique challenges of the surgical environment, such as the scarcity of annotated real-world data, the geometry of articulated instruments, and the presence of occlusions.

The core goal is to enable accurate pose estimation without extensive manual annotation of real surgical data. To achieve this, a three-component pipeline is proposed, consisting of synthetic data generation, a tailored pose estimation framework, and a training strategy that leverages both synthetic and real unannotated data.

## 2.2. Synthetic Data Generation

Synthetic data helps overcome the challenges associated with acquiring and annotating real-world data, which is particularly difficult in the surgical domain due to privacy concerns and the complexity of capturing ground truth poses.

### 2.2.1. 3D Modeling of Surgical Instruments

We decided to create our own CAD models of the surgical instruments instead of relying on existing CAD models. This decision was driven by the need for highly realistic and accurate representations, as well as the unavailability of CAD models.

To prepare surgical instruments for photogrammetry, we spray them with a dust spray to minimize glare and reflections that could interfere with the scanning process. We found that dry shampoo worked better as a dust spray than specialized sprays for 3D scanning. It resulted in a better 3D reconstruction and is more cost-effective. The tools are then placed on a spinning table and photographed 360 degrees at three different heights. This ensures that every detail and surface of the instruments is accurately captured.

The captured images are processed using Reality Capture [14], a professional photogrammetry software. Once the initial 3D meshes are generated, we perform a series of refinement steps to enhance their quality and realism. We use Blender [8], a popular free and open source 3D modeling and animation software, to clean the meshes by removing noise and artifacts introduced during the photogrammetry process. Additionally, we employ Blender’s smoothing and hole-filling tools to improve the mesh surface quality.

To simulate the articulation of the surgical instruments, we used two different techniques. For the needle holder, which consists of two rigid parts, we separated the model into two parts. For the tweezers, which are made from a single part, the opening and closing introduce bending. To simulate this bending, we used Blender’s rigging and weight-painting tools. Rigging involves creating a virtual skeleton within the 3D mesh, allowing us to define the movement of different parts. Weight painting assigns influence levels to the bones, which control how the mesh deforms when the bones move. This combination allows us to simulate the bending motion of the tweezers, ensuring realistic articulation.

Figure 4 shows the tools we scanned at different articulation angles. After rigging the meshes, we exported them in different articulation angles. Specifically, we exported 15 different meshes for the needle holder and 10 meshes for the tweezers, each representing a different articulation angle.

### 2.2.2. Hand-Object Interaction Modeling

Occlusions of hand grasps are commonly encountered in surgical scenarios. We simulate them with a generative hand-grasp model called ContactGen [36] in combination with the MANO hand mesh [48]. We used the model from the official implementation, which was trained on the GRAB dataset [54, 11]. The GRAB dataset includes real human grasps for 51 objects from 10 different subjects.

We generate a diverse set of hand-object grasps by varying the grip positions, hand orientations, and contact points between the hand and the surgical instruments. By incorporating

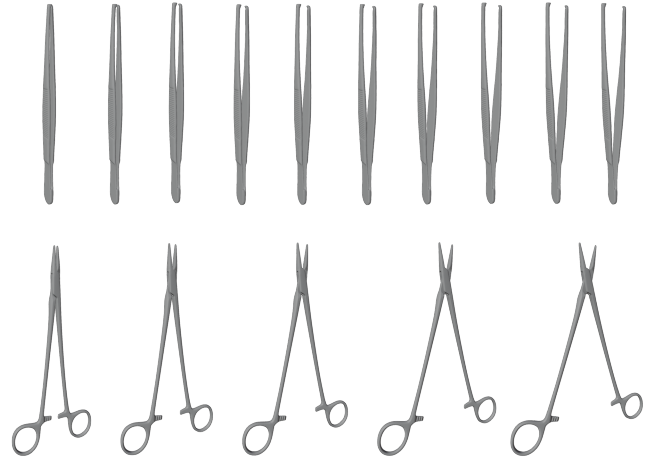


Fig. 4. Generated synthetic surgical tools in varying degrees of articulation

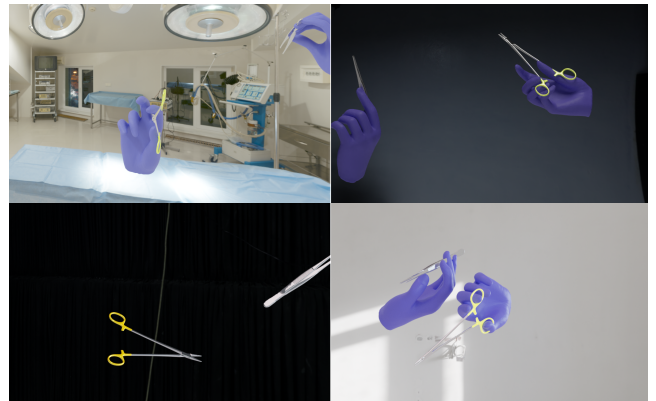


Fig. 5. Synthetic data of surgical tools

these hand-object grasps into our synthetic data, we introduce realistic hand occlusions and interactions.

### 2.2.3. Rendering Pipeline

With the rigged 3D models of the surgical instruments and the hand-object grasps, we proceed to render a large synthetic dataset using Blender. Our rendering pipeline generates diverse and realistic images with varying backgrounds and lighting conditions.

We create virtual environments within Blender, including operating room scenes and other indoor environments. To enhance the realism and variability of the rendered images, we incorporate HDRI (High Dynamic Range Imaging) maps, which provide high-quality lighting and reflections. These HDRI maps cover a wide range of lighting scenarios, from surgical settings to other indoor environments, adding diversity to our synthetic dataset.

During the rendering process, we randomize various aspects of the scene to increase the diversity of the synthetic dataset. This includes randomizing the positions and orientations of the surgical instruments, the hand-object grasps, and the camera viewpoints. We also apply random variations to the material properties of the instruments, such as their color and surface properties, to introduce visual variability.

In total, we generate 80,000 synthetic images using our rendering pipeline, utilizing BlenderProc [16]. Each image is accompanied by precise ground-truth annotations, including the 6D pose of the surgical instruments and the articulation angles. This comprehensive synthetic dataset serves as a valuable resource for training our pose estimation network. A sample from this dataset is illustrated in Figure 5.

### 2.3. Pose Estimation Framework

Our pose estimation framework follows a two-stage approach, consisting of an object detection stage followed by a pose estimation stage. The first stage involves detecting the objects of interest in the input image. The second stage takes the detected object crops and estimates the 6D pose, object class, and articulation angle.

The object detection stage is handled by YOLOv8 [27], which is trained to detect and localize the surgical tools in the input image. The detector provides bounding boxes around the detected tools, along with confidence scores indicating the likelihood of each surgical tool class.

The pose estimation stage takes as input cropped object regions from the detector and processes them through the pose estimation network. The pose estimation network estimates the 6D pose, object class, and articulation angle of the surgical tool.

#### 2.3.1. Direct 6D Object Pose Estimation

As briefly mentioned in 1, our pose estimation method draws inspiration from GDR-Net [60] for direct 6D object pose estimation, specifically the GDRNPP implementation [37], which incorporates several improvements over the original GDR-Net presented in the conference version. It is worth noting that GDRNPP won most awards in the 2022 BOP challenge [52] for “6D localization of seen objects” and “2D detection of seen objects”, demonstrating its state-of-the-art performance. We adopt several key components from GDR-Net, including the 3D rotation parameterization, 3D translation parameterization, 2D-3D dense correspondence maps, Patch-PnP, and the multitask 6D pose loss, which are described in the following paragraphs.

**3D Rotation Parameterization.** For the 3D rotation, we adopt the 6D rotation representation [67] instead of commonly used representations like quaternions or Euler angles. Quaternions and Euler angles suffer from ambiguities and discontinuities, which can hinder the learning process and lead to suboptimal pose estimates. The 6D rotation representation provides a continuous and unambiguous way to represent rotations.

The 6D rotation representation consists of two 3D vectors, denoted  $r_1$  and  $r_2$ , which correspond to the first two columns of the rotation matrix  $R \in SO(3)$ . The network predicts these two columns using the Patch-PnP module. To ensure the orthogonality and validity of the rotation matrix, Gram-Schmidt process is applied to the predicted columns. This process orthogonalizes the columns and computes the third column to complete the rotation matrix. The resulting rotation matrix  $R = [r_1, r_2, r_3]$  is guaranteed to be orthogonal and represents a valid 3D rotation.

In the context of working with object crops, we focus on predicting the allocentric representation of an object’s rotation

[29]. This approach is independent of the viewer’s perspective and assumes that the camera has rotated from its original position to point toward the center of the object’s Region of Interest (RoI). This representation eliminates the need to account for variable camera-object positioning, simplifying the rotational estimation process. Once the allocentric rotation is determined, it can be converted into the true 3D rotation (egocentric representation) by using the object’s 3D translation and the camera’s intrinsic parameters  $K$  [29].

**3D Translation Parameterization.** Direct prediction of translation from a Region of Interest (RoI) is impossible without additional information. To address this, we use a parametrization technique known as the scale-invariant translation estimate (SITE) [32]. SITE represents the translation as a combination of the 2D center coordinates of the object in the image plane and the depth of the object relative to the camera. The network predicts three components:  $(\delta_x, \delta_y, \delta_z)$ .

$\delta_x$  and  $\delta_y$  represent the offset of the object’s center with respect to the center of the bounding box in the image plane, normalized by the bounding size  $(w, h)$ . and  $\delta_z$  represents the depth of the object relative to the camera, normalized by the bounding box zoom-in ratio  $r = s_{\text{zoom}}/\max(w, h)$  where  $s_{\text{zoom}}$  is the crop zoom-in size.

To obtain the final 3D translation  $t = (t_x, t_y, t_z)$ , we first compute the 2D center coordinates of the object  $(o_x, o_y)$  by adding the predicted offsets  $(\delta_x, \delta_y)$  to the center of the bounding box  $(c_x, c_y)$ :

$$\begin{aligned} o_x &= c_x + \delta_x \cdot w \\ o_y &= c_y + \delta_y \cdot h \end{aligned}$$

Then, using the camera intrinsic parameters (focal length  $f$  and principal point  $(p_x, p_y)$ ), we compute the 3D translation:

$$\begin{aligned} t_x &= (o_x - p_x) \cdot \frac{t_z}{f} \\ t_y &= (o_y - p_y) \cdot \frac{t_z}{f} \\ t_z &= \delta_z \cdot r \end{aligned}$$

**2D-3D Dense Correspondence Maps.** The network generates a dense 2D-3D correspondence map [32, 24], which is an intermediate geometric feature that establishes a relationship between each object pixel in the 2D image and its corresponding 3D coordinate on the object model. These 3D coordinates are normalized using the dimensions of a tight 3D bounding box that encloses the mesh. Utilizing this correspondence map, we can apply PnP-RANSAC algorithms to find a plausible 6D pose of the object.

**Patch-PnP.** GDR-Net introduced a differentiable module named Patch-PnP, which is composed of convolutional layers followed by fully connected layers. This module processes geometric feature maps, such as 2D-3D Dense Correspondence Maps, and directly regresses the 6D object pose. Its primary aim is to replace the traditional PnP-RANSAC method with a more seamless and differentiable pipeline. The differentiable nature of Patch-PnP allows for end-to-end learning during the training of the pose estimation task.

### 2.3.2. Multitask Pose Losses

We utilize an ensemble of loss functions tailored to optimize different aspects of the 6D pose estimation task. The total loss comprises the following components:

*Pose Loss.* ( $\mathcal{L}_{\text{Pose}}$ ) This loss is further disentangled into three components:

- **Rotation Loss ( $\mathcal{L}_R$ ):** Measures the discrepancy between the predicted and ground-truth rotations using a point matching loss. The rotation loss is computed as:

$$\mathcal{L}_R = \frac{1}{N} \sum_{i=1}^N \|\hat{R}p_i - \bar{R}p_i\|_1$$

where  $\hat{R}$  is the estimated rotation matrix,  $\bar{R}$  is the ground truth rotation matrix,  $p_i$  are the 3D points in the object model, and  $N$  is the total number of points.

- **Center Loss ( $\mathcal{L}_{\text{center}}$ ):** L1 loss between the predicted and ground truth 2D center SITE components:

$$\mathcal{L}_{\text{center}} = \|(\hat{\delta}_x, \hat{\delta}_y) - (\bar{\delta}_x, \bar{\delta}_y)\|_1$$

- **Depth Loss ( $\mathcal{L}_z$ ):** L1 loss between the predicted and ground truth object centroid SITE component:

$$\mathcal{L}_z = \|\hat{\delta}_z - \bar{\delta}_z\|_1$$

*Geometry Loss ( $\mathcal{L}_{\text{Geom}}$ ).* This loss combines the dense correspondence loss and the mask losses:

- **Mask Loss ( $\mathcal{L}_{\text{mask}}$ ):** The mask loss consists of two terms, the visible mask loss and the amodal (full) mask loss:

$$\mathcal{L}_{\text{mask}} = \|\hat{M}_{\text{vis}} - \bar{M}_{\text{vis}}\|_1 + \|\hat{M}_{\text{full}} - \bar{M}_{\text{full}}\|_1$$

where  $M_{\text{vis}}$  is the visible object mask and  $M_{\text{full}}$  is the full object mask.

- **2D-3D Dense Correspondence Loss ( $\mathcal{L}_{\text{corr}}$ ):** L1 loss between the predicted and ground truth dense 2D-3D correspondence maps:

$$\mathcal{L}_{\text{corr}} = \frac{1}{\sum \bar{M}_{\text{vis}}} \|\bar{M}_{\text{vis}} \odot (\hat{D} - \bar{D})\|_1$$

where  $D$  is the 2D-3D dense correspondence, and  $\bar{M}_{\text{vis}}$  is the ground-truth visible object mask.

The total geometry loss is the sum of the dense correspondence loss and the mask loss:

$$\mathcal{L}_{\text{Geom}} = \mathcal{L}_{\text{corr}} + \mathcal{L}_{\text{mask}}$$

*Articulation Loss ( $\mathcal{L}_{\text{Art}}$ ).* L1 loss between the predicted and ground truth articulation angles.

$$\mathcal{L}_z = \|\hat{A} - \bar{A}\|_1$$

where  $A$  is the normalized articulation angle.

*Object Category Loss ( $\mathcal{L}_{\text{Cat}}$ ).* Cross-entropy loss of the object categories.

$$\mathcal{L}_{\text{Cat}} = \text{CE}(\hat{C}, \bar{C})$$

where  $C$  is the object class.

The total loss is a weighted sum of these individual loss components:

$$\mathcal{L}_{\text{total}} = w_{\text{Pose}} \cdot \mathcal{L}_{\text{Pose}} + w_{\text{Geom}} \cdot \mathcal{L}_{\text{Geom}} + w_{\text{Cat}} \cdot \mathcal{L}_{\text{Cat}} + w_{\text{Art}} \cdot \mathcal{L}_{\text{Art}} \quad (1)$$

### 2.3.3. Pose Model Architecture

Our pose estimation network simultaneously estimates object category, articulation angle, and pose from image crops. The network consists of two interconnected sections: (1) the intermediate feature regression stage and (2) the pose regression stage (Figure 6).

The intermediate feature regression stage is based on the Feature Pyramid Network (FPN) [33] with a Vision Transformer (ViT) backbone pretrained following the method described in [43] on the LVD-142M dataset. The features extracted by the ViT backbone are fed into a Pyramid Pooling Module (PPM) [66] before being fed back to the FPN. The object category head is attached to the PPM output for early branching [19]. The fused feature map from the FPN is directed to three heads: articulation, mask, and 2D-3D Dense Correspondence ( $M_{2D-3D}$ ).

The pose regression stage varies depending on the phase. During training, the  $M_{2D-3D}$  encoding is processed by Patch-PnP [60], a differentiable pose estimator. During testing, the  $M_{2D-3D}$  encoding is converted to 2D-3D pairs, and the pose is estimated using a PnP-RANSAC variant. The final output consists of the pose parameters ( $R_{3 \times 3}$ ,  $t_3$ ), object class, and articulation angle.

### 2.3.4. Training Procedure

The training process involves the following steps:

1. Train the pose estimation network and the object detection network independently on synthetic data.
2. Create pseudo-labels for the object detector using the pose estimation network and retrain the object detector on the pseudo-labels.
3. Create pseudo-labels for the pose estimator using the updated object detector and retrain the pose estimator on the pseudo-labels.
4. Repeat steps 2-3 for multiple iterations to progressively refine the networks' performance on real-world data.

The details of each step are discussed in the following subsections.

*Stage 1: Training on Synthetic Data.* In the first stage, we train the pose estimation network and the object detection network independently on the synthetic dataset generated using the pipeline described in Section 2.2.

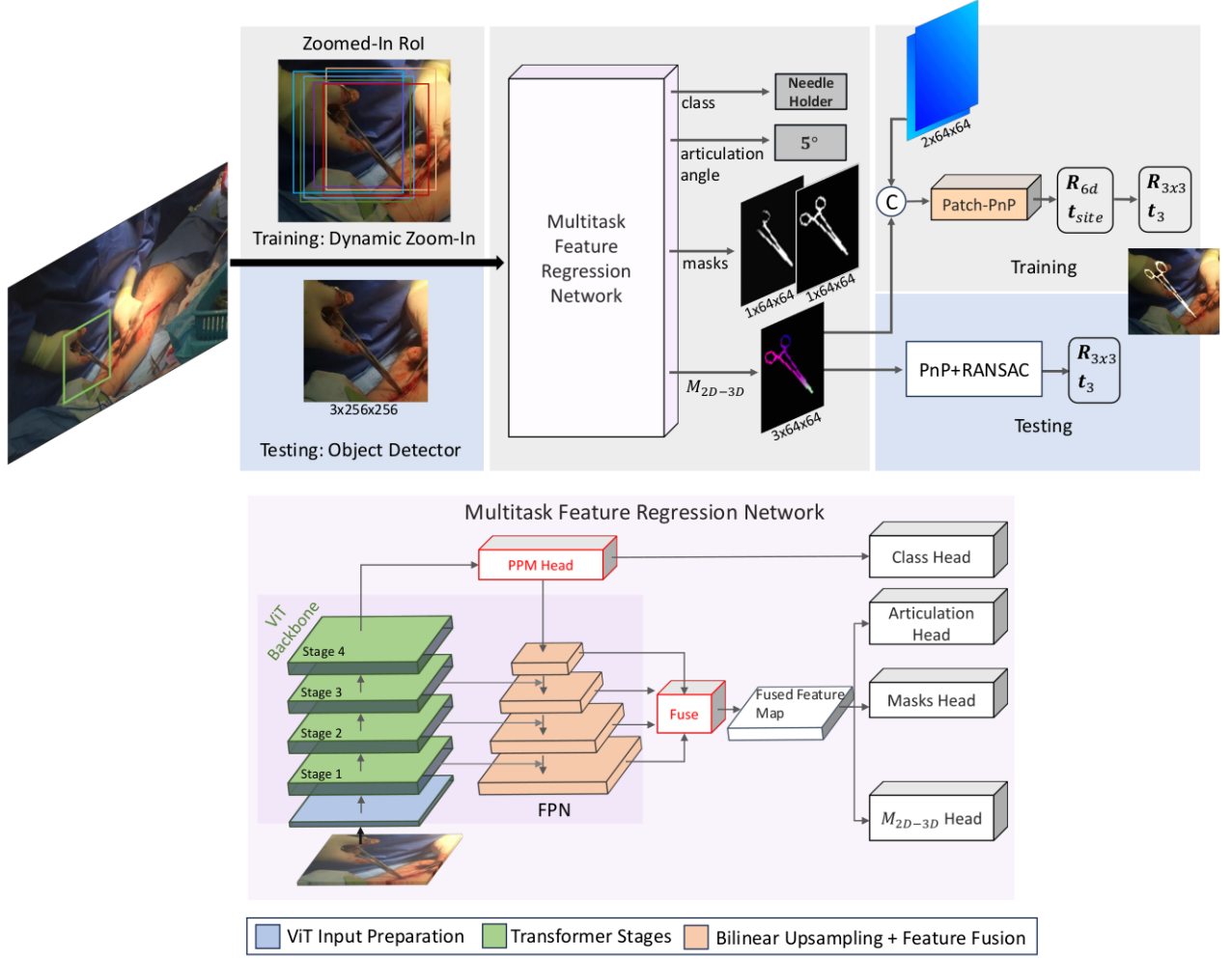


**Fig. 6. Pose Model Architecture:** The input image is cropped at the Region of Interest (RoI) and processed by the Multitask Feature Regression. The output,  $M_{2D-3D}$ , is then forwarded to Patch-PnP during training or to PnP-RANSAC during testing.

#### Step 2: Object Detection Domain Adaptation.

1. We apply object tracking on the real video data using the BoT-SORT [2] tracking algorithm.
2. We select frames with high detection confidence and at least three consecutive tracking detections as pseudo-labels for object detection.
3. The selected frames are passed to the pose estimator, which estimates the object pose, class, and articulation angle. The resulting mesh and pose are reprojected onto the image plane. The resulting reprojected bounding box is then used as the new pseudo-label for the object detection network. This process is illustrated in Figure 7.
4. Retrain the object detector on the pseudo-labeled data and a fraction of synthetic data.

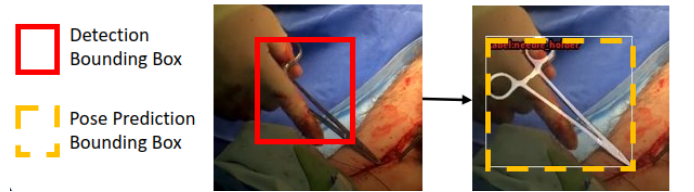


**Fig. 7. Bounding box refinement stage:** This figure illustrates the process of refining bounding boxes for object detection. Initially, frames with high detection confidence and consecutive tracking detections are selected. These frames are then passed to the pose estimator, which estimates the object pose, class, and articulation angle. The resulting mesh and pose are reprojected onto the image plane, creating a reprojected bounding box that is used as the new pseudo-label for retraining the object detection network.

#### Step 3: Pose Estimation Domain Adaptation.

1. Using the refined object detection model, we obtain image crops of the detected objects from the real video data.
2. We run the pose estimation network on these image crops to predict the 6D pose, object class, and articulation angle.

3. We filter the pose predictions based on the following criteria:

- High class confidence
- Low PnP-RANSAC outlier count
- Low reprojection error

The pose predictions that satisfy these criteria are selected as pseudo-labels for pose estimation.

4. Retrain the pose estimator on the pseudo-labeled data and a fraction of synthetic data.

### 3. Experiments, Results, and Ablation Studies

#### 3.1. Experimental Setup

Our experiments are implemented with the PyTorch deep learning framework. We train our models end-to-end using the Ranger optimizer [35, 65, 63], which combines Rectified Adam (RAdam) with Lookahead. A batch size of 120 is used during training, along with a base learning rate of  $1e-5$ . We employ a cosine annealing learning rate schedule [38], which gradually reduces the learning rate after approximately 72% of the training iterations.

During training, we apply various data augmentation techniques with a base probability of 0.8. These augmentations are taken from the GDRNPP implementation [60, 37] and include: Gaussian blur, Sharpness enhancement, Contrast enhancement, Brightness adjustment, Color enhancement, Addition of random values to pixel intensities, Channel-wise inversion, Multiplication of pixel intensities, Addition of Gaussian noise, Linear contrast adjustment, and Grayscale conversion.

For inference, we use the Progressive-X [6] PnP-RANSAC scheme, which utilizes Graph-Cut RANSAC [5].

##### 3.1.1. Dataset and Labels

As discussed in Section 1.6, our real-world dataset consists of annotated frames from seven different surgical procedures. For each surgery, approximately 100 images were selected and manually annotated with detailed segmentation masks of the surgical tools and hands. These annotations are used for testing only; they serve as the ground truth for evaluating our pose estimation method on real-world data.

##### 3.1.2. Evaluation Metrics

Due to the lack of ground truth 6D pose annotations in our real-world dataset, we employ a 2D reprojection-based evaluation method. This approach compares the reprojected mask of the object, obtained using the estimated pose, class, and articulation angle, with the manually annotated segmentation masks. However, directly comparing the full reprojection masks to the annotated tool masks may not provide an accurate assessment of the pose estimation accuracy, as the annotated tool masks may be partially occluded by the surgeon’s hands. To account for these occlusions, we incorporate the hand masks into our evaluation process.

**6D Pose Evaluation Metric.** We propose a hand-occlusion aware reprojection that focuses on evaluating the visible parts of the tools while considering the presence of hand occlusions. The steps involved in computing the metrics are as follows:

1. Given an input image and the estimated pose of the surgical tool, we project the 3D model of the tool onto the 2D image plane using the camera’s intrinsic parameters. This results in a reprojected binary mask representing the visible surface of the tool according to the estimated pose.

**Table 1. Pose Estimation Average Precision (AP) on the Real-World Surgical Data.** "Synth" refers to training on synthetic data, "Real" refers to refinement on real data, "GT RoI" refers to ground truth RoI, and "Pred RoI" refers to predicted RoI.

RoI	Trained on	Needle-holder	Tweezers	Mean
GT RoI	Synth	0.654	0.680	0.667
GT RoI	Real	0.784	0.805	0.795
Pred RoI	Real	0.754	0.752	0.753

2. We subtract the hand masks from both the annotated tool masks and the reprojected tool masks. This step removes the regions occluded by the hands, allowing us to focus on the visible parts of the tools.

We use the Average Precision (AP) metric for segmentation following the method used in the COCO 2020 Object Segmentation Challenge [34] and BOP 2022 Challenge [52]. For each object, we calculate a per-object Average Precision ( $AP_O$ ) by averaging the AP across the following Intersection over Union (IoU) thresholds: [0.5, 0.55, 0.6, 0.65, 0.7, 0.75, 0.8, 0.85, 0.9, 0.95]. The IoU is evaluated between the manually subtracted annotated tool mask and the manually subtracted reprojected tool mask. The overall performance metric (AP) is then computed by averaging the  $AP_O$  scores for all objects.

**2D Object Detection Metric.** Similarly to our segmentation approach, the AP is determined by calculating the precision at various IoU thresholds, yet here it specifically evaluates the accuracy with which objects are detected rather than segmented. The overall AP score reflects the aggregate precision across all detected objects in the dataset. We evaluate only those object instances where at least 10% of their projected surface area is visible, excluding detections of objects visible from less than 10% which are not counted towards false positives. Due to the lack of ground-truth poses and the minimal variation in camera-to-object distance, we estimate the visibility percentage of each object by counting the number of visible pixels in the ground truth segmentation.

##### 3.1.3. Results on Real-World Surgical Data

**Pose Estimation Results.** Table 1 presents the performance of our pose estimation method on the real-world surgical dataset. We evaluate the Average Precision (AP) for two surgical tools: needle-holder and tweezers. The AP is computed based on the hand-occlusion-aware reprojection metric described in the previous section.

We compare three variations of our method: (1) Pose estimation trained only on synthetic data, (2) Pose estimation with real data refinement. These variations are evaluated using both ground truth bounding boxes (GT Bbox) and predicted bounding boxes from the object detection stage. It is important to note that predicting pose on the ground truth bounding boxes isolates the pose estimation performance and does not introduce the errors caused by the bounding box prediction.

**Table 2. YOLOv8 Object Detection Average Precision on the Real-World Surgical Data**

Training Strategy	Needle-holder	Tweezers	Mean
trained on synthetic data	0.564	0.455	0.510
tuned on real data	0.731	0.807	0.769
pose refinement	<b>0.841</b>	<b>0.877</b>	<b>0.859</b>

*Object Detection Results.* Table 2 presents the object detection performance on the real-world surgical dataset. We evaluate the Average Precision (AP) for detecting the needle-holder and tweezers using our object detection method. We present results when training the model only on synthetic data, after refinement on real data and pose refinement with the tuned pose model as depicted in Figure 7.

### 3.2. Ablation Studies

#### 3.2.1. Impact of Synthetic Hand-Object Interactions

To investigate the impact of synthetic hand-object interactions on the performance of our pose estimation and object detection models, we conduct a series of ablation studies. We train three variants of our models on different synthetic datasets. These datasets are a sub-sample of the whole synthetic data that we generated:

1. Synthetic data with synthetic hands: This dataset includes realistic hand-object interactions, as described in Section 1.6.
2. Synthetic data with masked tools: In this dataset, regions of the surgical tools that would have been occluded by hands are masked out to simulate occlusions without explicitly modeling the hands.
3. Synthetic data without hands: Here, synthetic hands are excluded from the rendering process, leaving only the surgical tools visible in the scenes.

Figure 8 shows an example of the hand dataset. We evaluate the performance of the pose estimation model and the object detection model trained on each of these datasets.

We evaluate the pose estimation accuracy of the models trained on the three synthetic datasets when provided with ground truth to isolate the impact of the object detection stage.

**Table 3. AP Metrics for Pose Model Evaluation with Ground-Truth Bounding Boxes**

Synthetic Dataset	Needle-holder	Tweezers	Mean
Without Hands	0.483	0.621	0.552
Masked Tools	0.574	0.727	0.651
With Hands	<b>0.577</b>	<b>0.758</b>	<b>0.668</b>

#### 3.2.2. Patch-PnP vs. PnP-RANSAC

This ablation study evaluates the performance of two different strategies for pose estimation: Patch-PnP and PnP-RANSAC.

For PnP-RANSAC, we utilize the Progressive-x algorithm [6] in conjunction with Graph-cut RANSAC [5]. Hereafter, we refer to this combination as PnP-RANSAC. Progressive-x is a multi-model fitting algorithm that progressively fits model instances to data points, taking into account both the fit quality and the spatial coherence of the points. Graph-cut RANSAC is a variant of RANSAC that enhances the efficiency and robustness of model fitting through graph-based segmentation. It employs a graph-based representation of the data points and uses graph-cut optimization to identify the optimal set of inliers for each model hypothesis.

*Training strategy impact.* We evaluate the impact of training an end-to-end pose estimation model with Patch-PnP and all the associated pose losses as described in section 2.3.2, vs training without the Patch-PnP module. The inference strategy in both cases is with PnP-RANSAC. Results are shown in table 4.

**Table 4. Comparison of Patch-PnP and Prog-x with Graph-cut RANSAC for pose estimation inference.**

Strategy	Needle-holder	Tweezers	Mean
Patch-PnP	0.567	<b>0.803</b>	0.685
Prog-x	<b>0.671</b>	0.779	<b>0.725</b>

*Inference strategy impact.* In this experiment we evaluate PnP-RANSAC vs Patch-PnP inference on an end-to-end trained pose model. Results are shown in table 5.

**Table 5. Comparison of Patch-PnP and Prog-x with Graph-cut RANSAC for pose estimation inference.**

Strategy	Needle-holder	Tweezers	Mean
Patch-PnP	0.622	<b>0.839</b>	0.731
Prog-x	<b>0.784</b>	0.805	<b>0.795</b>

The results show that using PnP-RANSAC overall achieves better results than Patch-PnP, though on the Tweezers, Patch-PnP outperformed PnP-RANSAC.

## 4. Discussion and Conclusions

This study introduced a novel approach for monocular pose estimation of articulated surgical instruments in open surgery, marking an "in the wild" investigation in a relatively under-explored domain. Our approach involved creating a diverse synthetic dataset of surgical instruments with various articulation angles, enabling initial model training. These models were then refined through synthetic to real domain adaptation techniques, resulting in robust predictions of 6D pose, instrument class, and articulation angle in real surgical scenarios. The results demonstrate our method's effectiveness in addressing unique surgical environment challenges, such as limited real-world data, complex instrument geometry, and occlusions. Notably, our approach shows promise not only in pose estimation but also in improving object detection accuracy through an iterative refinement process that leverages our pose estimation

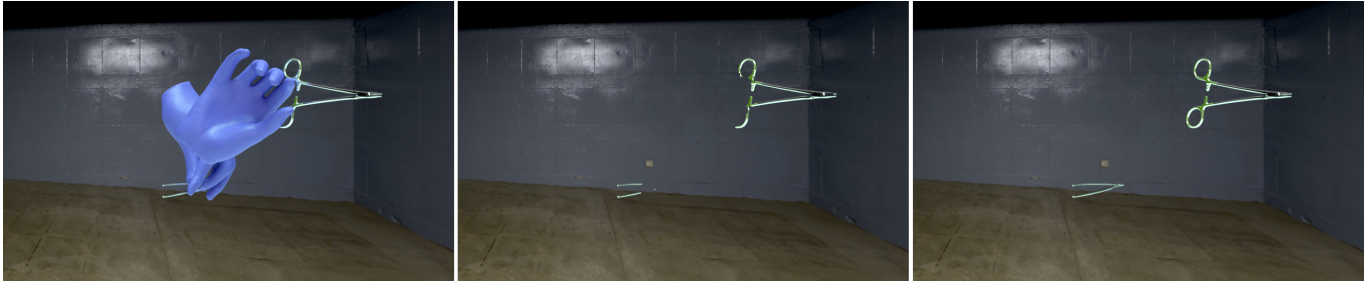


Fig. 8. Example from hand ablation data: image with synthetic hands (left), image with masked tools (middle), image without hands (right).

method, suggesting a potential pathway for enhancing overall surgical instrument recognition systems.

While our approach shows promise, we acknowledge certain limitations that present opportunities for future research. Our current evaluation method focuses on the 2D reprojection of estimated poses, which does not fully capture the depth information of the instruments. Future work could incorporate depth information in the evaluation process to enhance 3D position accuracy. Additionally, our study was limited to two surgical tools and one site, and expanding the synthetic dataset to include a wider variety of instruments would further demonstrate the generalizability of our approach.

Looking ahead, this work opens up several directions for future research in surgical instrument pose estimation. Future studies could explore a wider range of surgical instruments and environments to further test and refine these techniques. The potential for improving both pose estimation and object detection accuracy through our iterative approach also merits further investigation.

In conclusion, our study demonstrates a novel approach to pose estimation of articulated surgical instruments in open surgery using synthetic data and domain adaptation techniques. This work contributes to the ongoing efforts in computer-assisted surgery, offering a potential pathway to overcome the challenge of limited annotated real-world data. As research in this field progresses, we hope that this and similar approaches will continue to be refined, ultimately supporting the development of more effective tools for surgical assistance and training.

## References

- [1] Ababsa, F.e., Malle, M., 2004. Robust camera pose estimation using 2d fiducials tracking for real-time augmented reality systems, in: Proceedings of the 2004 ACM SIGGRAPH international conference on Virtual Reality continuum and its applications in industry, pp. 431–435.
- [2] Aharon, N., Orfaig, R., Bobrovsky, B.Z., 2022. Bot-sort: Robust associations multi-pedestrian tracking. arXiv preprint arXiv:2206.14651.
- [3] Allan, M., Shvets, A., Kurmann, T., Zhang, Z., Duggal, R., Su, Y.H., Rieke, N., Laina, I., Kalavakonda, N., Bodenstedt, S., et al., 2019. 2017 robotic instrument segmentation challenge. arXiv preprint arXiv:1902.06426.
- [4] Bai, T., Luo, J., Zhao, J., Wen, B., Wang, Q., 2021. Recent advances in adversarial training for adversarial robustness. arXiv preprint arXiv:2102.01356.
- [5] Barath, D., Matas, J., 2018. Graph-cut ransac, in: Proceedings of the IEEE conference on computer vision and pattern recognition, pp. 6733–6741.
- [6] Barath, D., Matas, J., 2019. Progressive-x: Efficient, anytime, multi-model fitting algorithm, in: Proceedings of the IEEE/CVF international conference on computer vision, pp. 3780–3788.
- [7] Bkheet, E., D’Angelo, A.L., Goldbraikh, A., Laufer, S., 2023. Using hand pose estimation to automate open surgery training feedback. International Journal of Computer Assisted Radiology and Surgery 18, 1279–1285.
- [8] Blender Foundation, 2023. Blender. URL: <https://www.blender.org/>. version 3.5.0.
- [9] Bouget, D., Allan, M., Stoyanov, D., Jannin, P., 2017. Vision-based and marker-less surgical tool detection and tracking: a review of the literature. Medical image analysis 35, 633–654.
- [10] Bouget, D., Benenson, R., Omran, M., Riffaud, L., Schiele, B., Jannin, P., 2015. Detecting surgical tools by modelling local appearance and global shape. IEEE transactions on medical imaging 34, 2603–2617.
- [11] Brahmabhatt, S., Ham, C., Kemp, C.C., Hays, J., 2019. ContactDB: Analyzing and predicting grasp contact via thermal imaging, in: The IEEE Conference on Computer Vision and Pattern Recognition (CVPR). URL: <https://contactdb.cc.gatech.edu>.
- [12] Braun, M., Rao, Q., Wang, Y., Flohr, F., 2016. Pose-rcnn: Joint object detection and pose estimation using 3d object proposals, in: 2016 IEEE 19th International Conference on Intelligent Transportation Systems (ITSC), IEEE. pp. 1546–1551.
- [13] Burton, W., Myers, C., Rutherford, M., Rullkoetter, P., 2023. Evaluation of single-stage vision models for pose estimation of surgical instruments. International Journal of Computer Assisted Radiology and Surgery 18, 2125–2142.
- [14] Capturing Reality, 2023. Reality capture. URL: <https://www.capturingreality.com/>.
- [15] Colleoni, E., Edwards, P., Stoyanov, D., 2020. Synthetic and real inputs for tool segmentation in robotic surgery, in: International Conference on Medical Image Computing and Computer-Assisted Intervention, Springer. pp. 700–710.
- [16] Denninger, M., Winkelbauer, D., Sundermeyer, M., Boerdijk, W., Knauer, M., Strobl, K.H., Humt, M., Triebel, R., 2023. Blenderproc2: A procedural pipeline for photorealistic rendering. Journal of Open Source Software 8, 4901. URL: <https://doi.org/10.21105/joss.04901>, doi:10.21105/joss.04901.
- [17] Doignon, C., Nageotte, F., Maurin, B., Krupa, A., 2008. Pose estimation and feature tracking for robot assisted surgery with medical imaging. Unifying perspectives in computational and robot vision , 79–101.
- [18] Elfiring, R., de la Fuente, M., Radermacher, K., 2010. Assessment of optical localizer accuracy for computer aided surgery systems. Computer Aided Surgery 15, 1–12.
- [19] Elhoseiny, M., El-Gaaly, T., Bakry, A., Elgammal, A., 2015. Convolutional models for joint object categorization and pose estimation. arXiv preprint arXiv:1511.05175.
- [20] Ganin, Y., Ustinova, E., Ajakan, H., Germain, P., Larochelle, H., Laviolette, F., March, M., Lempitsky, V., 2016. Domain-adversarial training of neural networks. Journal of machine learning research 17, 1–35.
- [21] Hasan, M.K., Calvet, L., Rabbani, N., Bartoli, A., 2021. Detection, segmentation, and 3d pose estimation of surgical tools using convolutional neural networks and algebraic geometry. Medical Image Analysis 70, 101994.
- [22] He, K., Gkioxari, G., Dollár, P., Girshick, R., 2017. Mask r-cnn, in: Proceedings of the IEEE international conference on computer vision, pp. 2961–2969.
- [23] Hein, J., Seibold, M., Bogo, F., Farshad, M., Pollefeys, M., Furstahl, P.,

- Navab, N., 2021. Towards markerless surgical tool and hand pose estimation. *International journal of computer assisted radiology and surgery* 16, 799–808.
- [24] Hodan, T., Barath, D., Matas, J., 2020. Epos: Estimating 6d pose of objects with symmetries, in: *Proceedings of the IEEE/CVF conference on computer vision and pattern recognition*, pp. 11703–11712.
- [25] Hodan, T., Michel, F., Brachmann, E., Kehl, W., GlentBuch, A., Kraft, D., Drost, B., Vidal, J., Ihrke, S., Zabulis, X., et al., 2018. Bop: Benchmark for 6d object pose estimation, in: *Proceedings of the European conference on computer vision (ECCV)*, pp. 19–34.
- [26] Hodaň, T., Sundermeyer, M., Drost, B., Labbé, Y., Brachmann, E., Michel, F., Rother, C., Matas, J., 2020. Bop challenge 2020 on 6d object localization, in: *Computer Vision—ECCV 2020 Workshops: Glasgow, UK, August 23–28, 2020, Proceedings, Part II* 16, Springer. pp. 577–594.
- [27] Jocher, G., Chaurasia, A., Qiu, J., 2023. Ultralytics YOLO. URL: <https://github.com/ultralytics/ultralytics>.
- [28] Kirillov, A., Mintun, E., Ravi, N., Mao, H., Rolland, C., Gustafson, L., Xiao, T., Whitehead, S., Berg, A.C., Lo, W.Y., Dollár, P., Girshick, R., 2023. Segment anything. *arXiv:2304.02643*.
- [29] Kundu, A., Li, Y., Rehg, J.M., 2018. 3d-rcnn: Instance-level 3d object reconstruction via render-and-compare, in: *Proceedings of the IEEE conference on computer vision and pattern recognition*, pp. 3559–3568.
- [30] Labbé, Y., Carpentier, J., Aubry, M., Sivic, J., 2020. Cosypose: Consistent multi-view multi-object 6d pose estimation, in: *Computer Vision—ECCV 2020: 16th European Conference, Glasgow, UK, August 23–28, 2020, Proceedings, Part XVII* 16, Springer. pp. 574–591.
- [31] Lepetit, V., Pilet, J., Fua, P., 2004. Point matching as a classification problem for fast and robust object pose estimation, in: *Proceedings of the 2004 IEEE Computer Society Conference on Computer Vision and Pattern Recognition, 2004. CVPR 2004.*, IEEE. pp. II–II.
- [32] Li, Z., Wang, G., Ji, X., 2019. Cdpn: Coordinates-based disentangled pose network for real-time rgb-based 6-dof object pose estimation, in: *Proceedings of the IEEE/CVF International Conference on Computer Vision*, pp. 7678–7687.
- [33] Lin, T.Y., Dollár, P., Girshick, R., He, K., Hariharan, B., Belongie, S., 2017. Feature pyramid networks for object detection, in: *Proceedings of the IEEE conference on computer vision and pattern recognition*, pp. 2117–2125.
- [34] Lin, T.Y., Maire, M., Belongie, S., Hays, J., Perona, P., Ramanan, D., Dollár, P., Zitnick, C.L., 2014. Microsoft coco: Common objects in context, in: *Computer Vision—ECCV 2014: 13th European Conference, Zurich, Switzerland, September 6–12, 2014, Proceedings, Part V* 13, Springer. pp. 740–755.
- [35] Liu, L., Jiang, H., He, P., Chen, W., Liu, X., Gao, J., Han, J., 2019. On the variance of the adaptive learning rate and beyond. *arXiv preprint arXiv:1908.03265*.
- [36] Liu, S., Zhou, Y., Yang, J., Gupta, S., Wang, S., 2023. Contactgen: Generative contact modeling for grasp generation, in: *Proceedings of the IEEE/CVF International Conference on Computer Vision*, pp. 20609–20620.
- [37] Liu, X., Zhang, R., Zhang, C., Fu, B., Tang, J., Liang, X., Tang, J., Cheng, X., Zhang, Y., Wang, G., Ji, X., 2022. Gdrnp. [https://github.com/shanice-1/gdrnp\\_bop2022](https://github.com/shanice-1/gdrnp_bop2022).
- [38] Loshchilov, I., Hutter, F., 2016. Sgdr: Stochastic gradient descent with warm restarts. *arXiv preprint arXiv:1608.03983*.
- [39] Meza, J., Romero, L.A., Marrugo, A.G., 2021. Markerpose: robust real-time planar target tracking for accurate stereo pose estimation, in: *Proceedings of the IEEE/CVF Conference on Computer Vision and Pattern Recognition*, pp. 1282–1290.
- [40] Miller, A.T., Allen, P.K., 2004. Graspit! a versatile simulator for robotic grasping. *IEEE Robotics & Automation Magazine* 11, 110–122.
- [41] Mousavian, A., Anguelov, D., Flynn, J., Kosecka, J., 2017. 3d bounding box estimation using deep learning and geometry, in: *Proceedings of the IEEE conference on Computer Vision and Pattern Recognition*, pp. 7074–7082.
- [42] Nema, S., Vachhani, L., 2022. Surgical instrument detection and tracking technologies: Automating dataset labeling for surgical skill assessment. *Frontiers in Robotics and AI* 9, 1030846.
- [43] Oquab, M., Darcet, T., Moutakanni, T., Vo, H., Szafraniec, M., Khalidov, V., Fernandez, P., Haziza, D., Massa, F., El-Nouby, A., et al., 2023. Dino v2: Learning robust visual features without supervision. *arXiv preprint arXiv:2304.07193*.
- [44] Park, K., Patten, T., Vincze, M., 2019. Pix2pose: Pixel-wise coordinate regression of objects for 6d pose estimation, in: *Proceedings of the IEEE/CVF International Conference on Computer Vision*, pp. 7668–7677.
- [45] Payet, N., Todorovic, S., 2011. From contours to 3d object detection and pose estimation, in: *2011 International Conference on Computer Vision*, IEEE. pp. 983–990.
- [46] Peng, S., Liu, Y., Huang, Q., Zhou, X., Bao, H., 2019. Pvnnet: Pixel-wise voting network for 6dof pose estimation, in: *Proceedings of the IEEE/CVF conference on computer vision and pattern recognition*, pp. 4561–4570.
- [47] Rad, M., Lepetit, V., 2017. Bb8: A scalable, accurate, robust to partial occlusion method for predicting the 3d poses of challenging objects without using depth, in: *Proceedings of the IEEE international conference on computer vision*, pp. 3828–3836.
- [48] Romero, J., Tzionas, D., Black, M.J., 2017. Embodied hands: Modeling and capturing hands and bodies together. *ACM Transactions on Graphics, (Proc. SIGGRAPH Asia)* 36.
- [49] Romero, J., Tzionas, D., Black, M.J., 2022. Embodied hands: Modeling and capturing hands and bodies together. *arXiv preprint arXiv:2201.02610*.
- [50] Su, Y., Rambach, J., Minaskan, N., Lesur, P., Pagani, A., Stricker, D., 2019. Deep multi-state object pose estimation for augmented reality assembly, in: *2019 IEEE International Symposium on Mixed and Augmented Reality Adjunct (ISMAR-Adjunct)*, IEEE. pp. 222–227.
- [51] Su, Y., Saleh, M., Fetzter, T., Rambach, J., Navab, N., Busam, B., Stricker, D., Tombari, F., 2022. Zebropose: Coarse to fine surface encoding for 6dof object pose estimation, in: *Proceedings of the IEEE/CVF Conference on Computer Vision and Pattern Recognition*, pp. 6738–6748.
- [52] Sundermeyer, M., Hodaň, T., Labbe, Y., Wang, G., Brachmann, E., Drost, B., Rother, C., Matas, J., 2023. Bop challenge 2022 on detection, segmentation and pose estimation of specific rigid objects, in: *Proceedings of the IEEE/CVF Conference on Computer Vision and Pattern Recognition*, pp. 2784–2793.
- [53] Sundermeyer, M., Marton, Z.C., Durner, M., Triebel, R., 2020. Augmented autoencoders: Implicit 3d orientation learning for 6d object detection. *International Journal of Computer Vision* 128, 714–729.
- [54] Taheri, O., Ghorbani, N., Black, M.J., Tzionas, D., 2020. GRAB: A dataset of whole-body human grasping of objects, in: *European Conference on Computer Vision (ECCV)*. URL: <https://grab.is.tue.mpg.de>.
- [55] Tobin, J., Fong, R., Ray, A., Schneider, J., Zaremba, W., Abbeel, P., 2017. Domain randomization for transferring deep neural networks from simulation to the real world, in: *2017 IEEE/RSJ international conference on intelligent robots and systems (IROS)*, IEEE. pp. 23–30.
- [56] Tremblay, J., Prakash, A., Acuna, D., Brophy, M., Jampani, V., Anil, C., To, T., Cameracci, E., Boochoon, S., Birchfield, S., 2018a. Training deep networks with synthetic data: Bridging the reality gap by domain randomization, in: *Proceedings of the IEEE conference on computer vision and pattern recognition workshops*, pp. 969–977.
- [57] Tremblay, J., To, T., Sundaralingam, B., Xiang, Y., Fox, D., Birchfield, S., 2018b. Deep object pose estimation for semantic robotic grasping of household objects. *arXiv preprint arXiv:1809.10790*.
- [58] Tsai, C.Y., Hsu, K.J., Nisar, H., 2018. Efficient model-based object pose estimation based on multi-template tracking and pnp algorithms. *Algorithms* 11, 122.
- [59] Wang, C., Xu, D., Zhu, Y., Martín-Martín, R., Lu, C., Fei-Fei, L., Savarese, S., 2019. Densefusion: 6d object pose estimation by iterative dense fusion, in: *Proceedings of the IEEE/CVF conference on computer vision and pattern recognition*, pp. 3343–3352.
- [60] Wang, G., Manhardt, F., Tombari, F., Ji, X., 2021. Gdr-net: Geometry-guided direct regression network for monocular 6d object pose estimation, in: *Proceedings of the IEEE/CVF Conference on Computer Vision and Pattern Recognition*, pp. 16611–16621.
- [61] Wei, G.Q., Arbter, K., Hirzinger, G., 1997. Real-time visual servoing for laparoscopic surgery: controlling robot motion with color image segmentation. *IEEE Engineering in Medicine and Biology Magazine* 16, 40–45.
- [62] Xiang, Y., Schmidt, T., Narayanan, V., Fox, D., 2017. Posecnn: A convolutional neural network for 6d object pose estimation in cluttered scenes. *arXiv preprint arXiv:1711.00199*.
- [63] Yong, H., Huang, J., Hua, X., Zhang, L., 2020. Gradient centralization: A new optimization technique for deep neural networks, in: *Computer*

Vision–ECCV 2020: 16th European Conference, Glasgow, UK, August 23–28, 2020, Proceedings, Part I 16, Springer. pp. 635–652.

- [64] Zakharov, S., Shugurov, I., Ilic, S., 2019. Dpod: 6d pose object detector and refiner, in: Proceedings of the IEEE/CVF international conference on computer vision, pp. 1941–1950.
- [65] Zhang, M., Lucas, J., Ba, J., Hinton, G.E., 2019. Lookahead optimizer: k steps forward, 1 step back. *Advances in neural information processing systems* 32.
- [66] Zhao, H., Shi, J., Qi, X., Wang, X., Jia, J., 2017. Pyramid scene parsing network, in: Proceedings of the IEEE conference on computer vision and pattern recognition, pp. 2881–2890.
- [67] Zhou, Y., Barnes, C., Lu, J., Yang, J., Li, H., 2019. On the continuity of rotation representations in neural networks, in: Proceedings of the IEEE/CVF conference on computer vision and pattern recognition, pp. 5745–5753.